RSC Advances

PAPER

View Article Online
View Journal | View Issue

Cite this: *RSC Adv.*, 2018, **8**, 32221

Facile preparation of rGO/MFe_2O_4 (M = Cu, Co, Ni) nanohybrids and its catalytic performance during the thermal decomposition of ammonium perchlorate

Weiran Wang and Dongxiang Zhang*

Received 23rd May 2018
Accepted 28th July 2018

DOI: 10.1039/c8ra04412k

rsc.li/rsc-advances

Reduced graphene oxide/metal ferrite (rGO/MFe_2O_4, M = Cu, Co, Ni) nanohybrids are successfully prepared through a simple, one-step hydrothermal method. The rGO/MFe_2O_4 nanohybrids are characterized by XRD, TEM, FT-IR, XPS, Raman and BET surface area measurements. The rGO/MFe_2O_4 nanohybrids demonstrate amazing catalytic activities on the thermal decomposition of ammonium perchlorate (AP). DSC results indicate that rGO/MFe_2O_4 nanohybrids (3 wt%), could decrease the decomposition temperature of pure AP from 424.7 °C to 329.1 °C, 338.3 °C, and 364.8 °C, respectively. This enhanced catalytic performance is mainly attributed to the synergistic effect of NPs and rGO. The activation energy (E_a) of AP mixed with nanohybrids is investigated by two isoconversion methods, Flynne–Walle–Ozawa (FWO) and Kissinger–Akahira–Sunose (KAS), on a conversion degree (α) range from 0.05 to 0.95. The values of E_a calculated from the above two methods matched with each other. A strong dependence of E_a on α is observed, indicating a complex decomposition process.

1. Introduction

Ammonium perchlorate (AP) is the most common energetic oxidant in composite solid propellants (CSPs). The thermal decomposition characteristics of AP directly influence the burning behavior of CSPs.[1,2] Extensive studies reveal the catalytic activity of transition metals oxides which can significantly improve the performance of the decomposition of AP.[3–9] Among the numerous varieties of transition metals oxides, spinel oxides (nanoferrites) due to their size, surface site and abundance of cations, for co-ordination sites, can increase activity of chemical reactivity[10] and are widely applied in the fields of electronics, catalysis, adsorbents, *etc.* Previous studies have suggested that the increase of specific surface area of a catalyst would dramatically enhance its catalytic performance on thermal decomposition of AP.[11,12] However, nanoparticles (NPs) are likely to aggregate due to their large surface energy, which will lead to the decrease of specific surface area and further influence their catalytic performance in the decomposition process.

Enormous attention has been attracted on graphene due to its excellent special surface properties, high conductivity and thermal stability.[13,14] It has been proved that the two-dimensional structure of graphene sheets allows them to be the perfect dispersing-substrate for the NPs and acts as efficient solid conductive supporters for enabling good contact between nanoferrites.[15]

Herein, we prepared rGO/MFe_2O_4 (M = Cu, Co, Ni) nanohybrids in a facile one-pot way. We demonstrated a comparative study about the catalytic activities of nanohybrids on thermal decomposition of AP. As far as we know, no study involving rGO/MFe_2O_4 nanohybrids as a series of catalysts for the decomposition of AP has been reported.

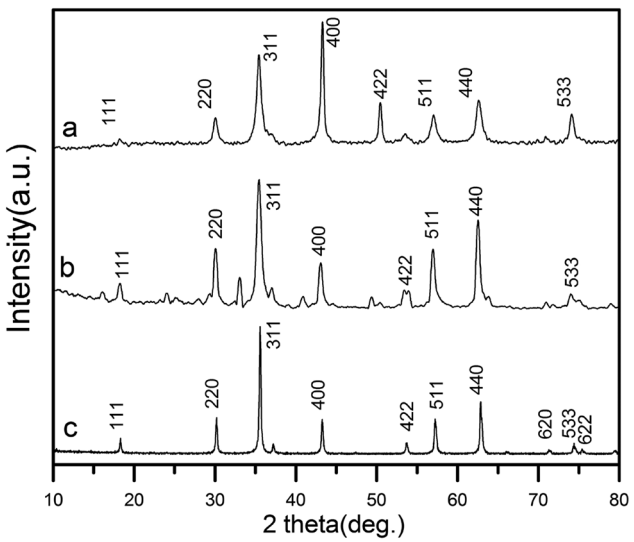

Fig. 1 XRD patterns of (a) rGO/CuF, (b) rGO/CoF, (c) rGO/NiF nanohybrids.

College of Chemistry and Chemical Engineering, Beijing Institute of Technology, Beijing 100081, P. R. China. E-mail: boris@bit.edu.cn; Fax: +86-10-68941331; Tel: +86-10-68914503

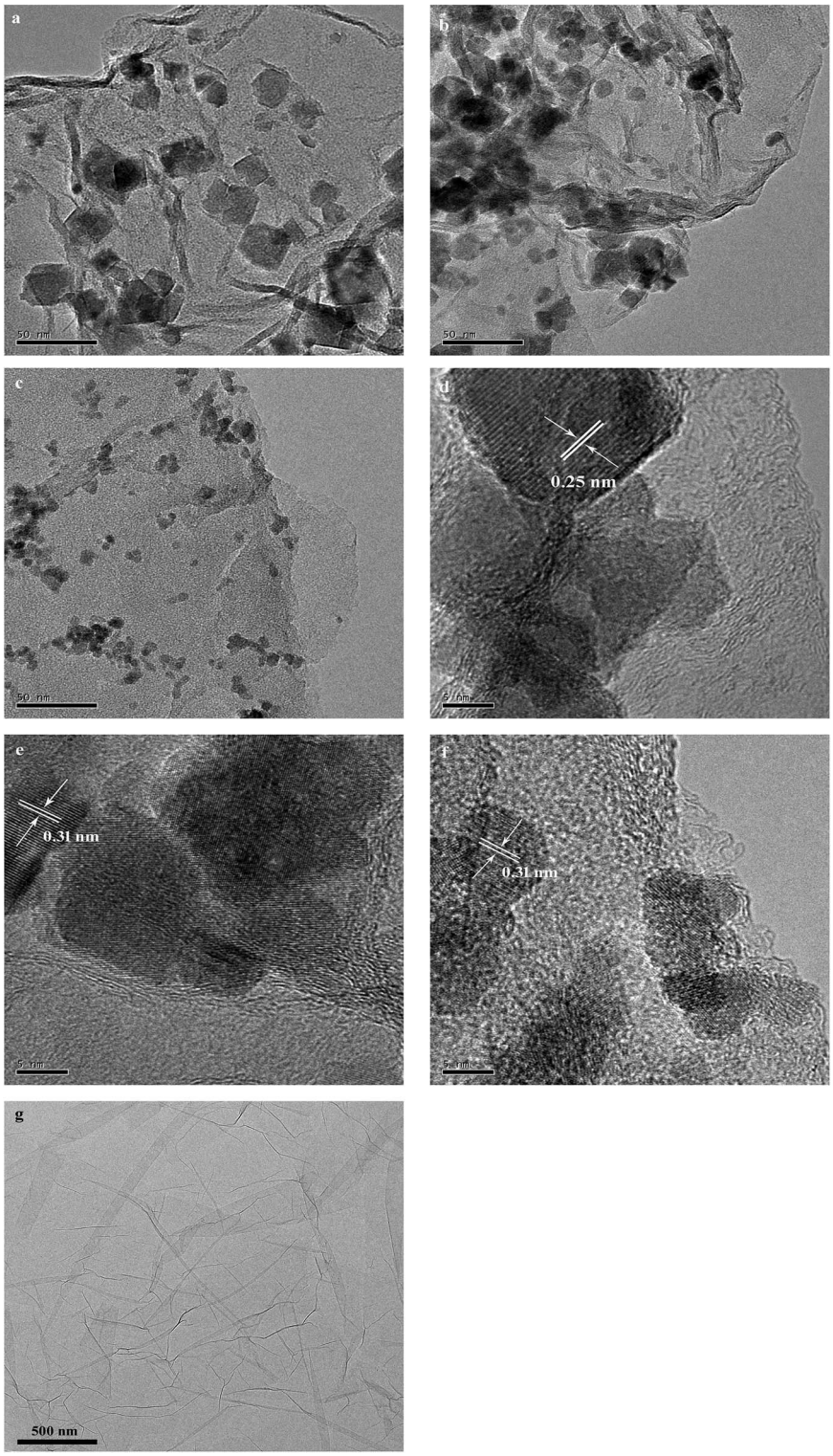

Fig. 2 TEM images of (a) rGO/CuF, (b) rGO/CoF, (c) rGO/NiF nanohybrids and (g) GO; HRTEM images of (d) rGO/CuF, (e) rGO/CoF, (f) rGO/NiF nanohybrids.

2. Experimental

2.1 Materials

Natural graphite powder was from Qingdao Graphite Factory. Potassium permanganate, sodium nitrate, concentrated sulfuric acid, hydrogen peroxide (30%), hydrochloric acid, sodium hydroxide anhydrous, ethanol, nitrates of Cu, Co, Ni and Fe were obtained from Beijing Chemical Reagent Co. Ltd. All reagents used are analytical grade.

2.2 Synthesis of rGO/MFe_2O_4 (M = Cu, Co, Ni) nanohybrids

GO was obtained from graphite powder in a modified Hummers way.[16] GO (72 mg) was added into deionized water (30 mL) with sonication. $M(NO_3)_2 \cdot nH_2O$ (M = Cu, Co, Ni) (1 mmol) and $Fe(NO_3)_3 \cdot 9H_2O$ (2 mmol) was mixed into GO solution. The mixtures were added with NaOH solution until a pH value of 11–12 reached under magnetic stirring. The viscous precipitates were moved into a 100 mL Teflon lined stainless-steel autoclave, heated overnight at 180 °C. The precipitates were centrifuged, rinsed with DI water and ethanol. The products labeled as rGO/CuF, rGO/CoF, rGO/NiF with rGO content of 25 wt%, were put in oven at 60 °C. For comparison, same process was repeated to prepare pure CuF, CoF, NiF NPs and graphene.

2.3 Characterization

X-ray powder diffraction (XRD) patterns of the nanohybrids were obtained using a Bruker D8-Advanced diffractometer. Transmission electron microscopy (TEM) and high-resolution (HRTEM) was measured on a JEOL, JEM-2100. The function groups were investigated by Fourier transform infrared spectra (FT-IR; Perkin Elmer). Raman spectra were investigated by a Raman spectrometer (Horiba JY HR-800). X-ray photoelectron spectroscopy (XPS) was characterized by a PHI Quantera system. Nitrogen adsorption/desorption isotherms were characterized by an BELSORP-max (ANKERSMID), Brunauer–Emmett–Teller (BET) method was used to calculate the specific surface area.

The rGO/MFe_2O_4 (M = Cu, Co, Ni) nanohybrids, rGO and pure MF NPs were fully mixed with AP in the mass ratio of 1 wt%, 3 wt% and 5 wt%, respectively. The thermal properties of the above mixtures were investigated using a differential thermal analyzer (TGA-DSC, METTLER, 1/1600HT) with nitrogen gas (flow rate 50 mL min^{-1}).

3. Results and discussion

3.1 Characterization

The XRD patterns of as-prepared rGO/CuF, rGO/CoF, rGO/NiF nanohybrids are displayed in Fig. 1. For $CuFe_2O_4$ (Fig. 1a), the peaks are at 2θ = 18.2°, 30.1°, 35.5°, 43.2°, 53.6°, 57.0°, 62.6°, 74.1°, which correspond to the crystal planes of (111), (220), (311), (400), (422), (511), (440), (533), respectively. The positions of all diffraction peaks (Fig. 1a–c) can be well assigned to standard structure of $CuFe_2O_4$, $CoFe_2O_4$, $NiFe_2O_4$ (JCPDS no. 77-0010, 22-1086 and 86-2267), respectively. The average crystallite size of rGO/CuF, rGO/CoF, rGO/NiF nanohybrids, calculated from the three most intense peaks of each patterns by Scherrer equation[17] are 15.3, 12.6, and 9.8 nm, respectively.

The morphology of the as-synthesised rGO/CuF, rGO/CoF, rGO/NiF nanohybrids and GO were characterized by TEM. As shown in Fig. 2a–c, MFe_2O_4 (M = Cu, Co, Ni) NPs are uniformly dispersed on rGO sheets. There are no NPs fell off the rGO sheets after long time sonication of the samples, indicating the strong interaction between NPs and rGO sheets. Fig. 2g shows a wrinkled waves-like textures of GO sheets. The HRTEM images of CuF, CoF, NiF NPs, presented in Fig. 2d–f, display a clear crystal lattice with a spacing of 0.25 nm, 0.31 nm, 0.31 nm, respectively, corresponding to (311), (111), (111) plane of MFe_2O_4 (M = Cu, Co, Ni) cubic structure.

Fig. 3 represents FTIR spectra of GO and rGO/MFe_2O_4 (M = Cu, Co, Ni). For GO (Fig. 3a), the broad absorption at 3411 cm^{-1} is ascribed to O–H stretching mode. The other peaks are due to the stretching vibration of carboxylic C=O (1735 cm^{-1}), aromatic C–C (1617 cm^{-1}), C–OH (1407 cm^{-1}), C–O–C (1214 cm^{-1}) and alkoxy (1049 cm^{-1}), respectively.[18] For rGO/MFe_2O_4 (Fig. 3b–d), peak intensity of oxygen-containing groups decreased obviously or disappeared gradually indicating that GO has been successfully reduced to rGO.[19] The peak at 1574 cm^{-1}, is due to the skeletal vibration of rGO sheets. A new absorption at around 600 cm^{-1} is assigned to the metal oxygen bonds.

Fig. 4 displays the XPS spectra of rGO/MFe_2O_4 (M = Cu, Co, Ni) nanohybrids and GO. Fig. 4a is clearly indicated that the C/O ratios in the rGO/MFe_2O_4 nanohybrids increase obviously compared with that of GO. In Fig. 4b, the peaks at around 723.0 and 710.6 eV corresponds to $Fe2p_{1/2}$ and $Fe2p_{3/2}$, respectively.[20] In Fig. 4c–e, two peaks at 932.9 eV and 952.7 eV are assigned to $Cu2p_{1/2}$ and $Cu2p_{3/2}$, respectively.[21] Two peaks at 779.2 eV and 880.8 eV is ascribed to the Co $2p_{3/2}$ and $Co2p_{1/2}$, respectively.[22] Two peaks at 855.0 and 872.7 eV corresponds to $Ni2p_{3/2}$ and $Ni2p_{1/2}$, respectively.[23] In Fig. 4f, four peaks at 284.1, 286.3, 287.5, 288.7 eV assigned to aromatic C=C/C–C, C–OH, C=O, O=C–O bonds, respectively.[24] Fig. 4g–i show that peak intensities of the epoxide and hydroxyl functional groups are remarkably decreased, suggesting the successful reduction of GO.

Fig. 5 displays Raman spectra of GO and rGO/MF (M = Cu, Co, Ni) nanohybrids. As can be seen in Fig. 5a, two peaks at around 1356 cm^{-1} and 1597 cm^{-1} corresponding to D and G band, respectively. In Fig. 5b and c, small shifting was seen in D and G bands suggesting oxygen-containing functional groups of GO are remarkably removed. The calculated intensity ratios of D and G band (I_D/I_G) of rGO/CuF, rGO/CoF, rGO/NiF and GO are 1.07, 1.09, 1.04, 0.90, respectively. The higher I_D/I_G values of rGO/MF nanohybrids suggest that GO sheets are successfully reduced.[25]

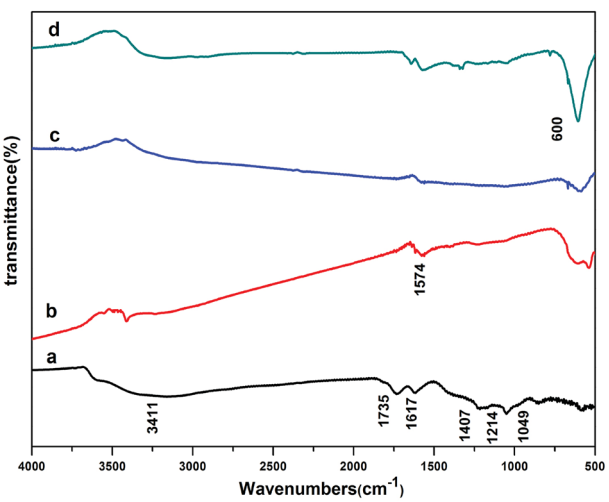

Fig. 3 FT-IR absorption spectra of (a) GO, (b) rGO/CuF, (c) rGO/CoF, (d) rGO/NiF nanohybrids.

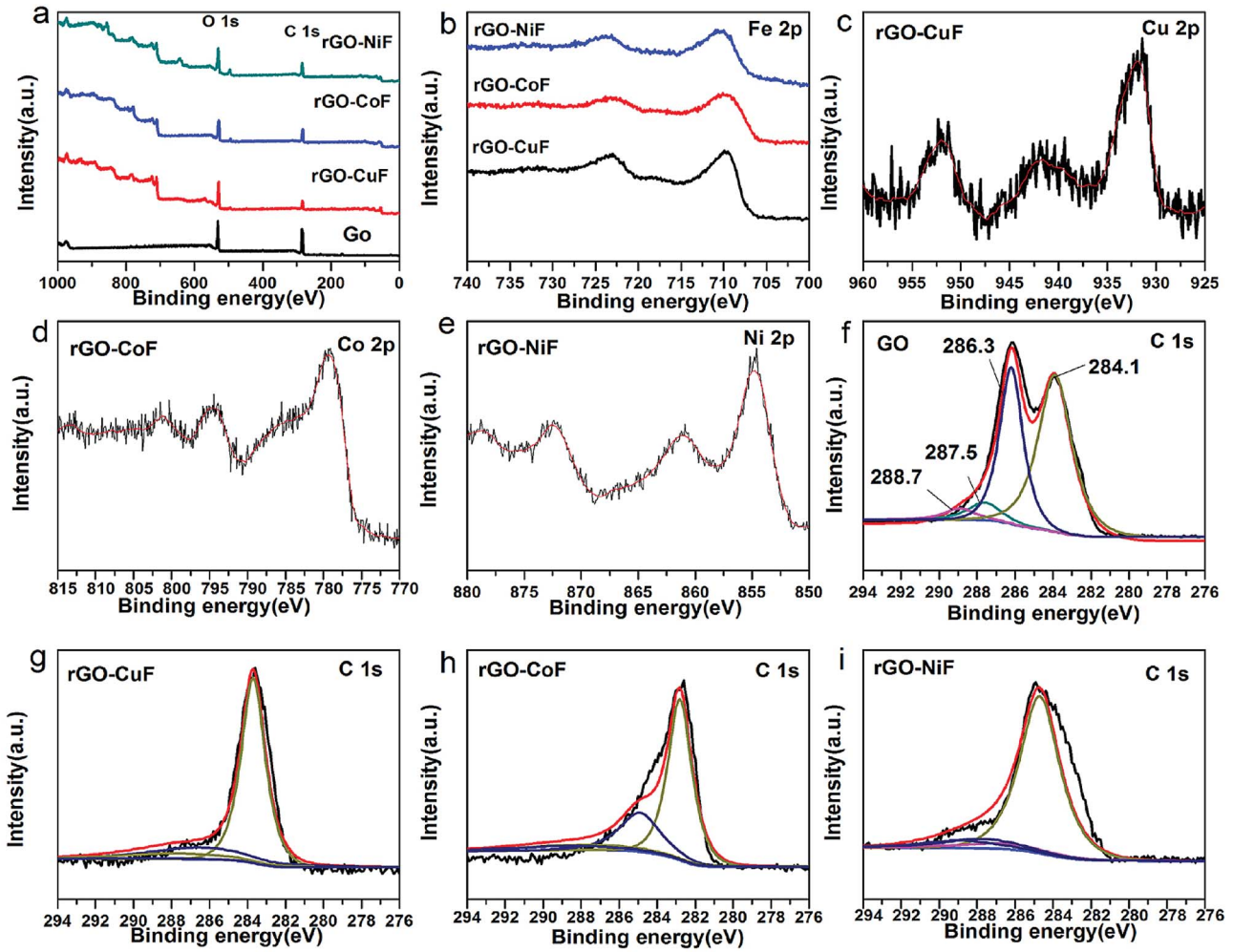

Fig. 4 XPS spectra of the rGO/MFe_2O_4 (M = Cu, Co, Ni) nanohybrids and GO (a) survey, (b) Fe 2p, (c) Cu 2p, (d) Co 2p, (e) Ni 2p, (f) C 1s, (g) C 1s, (h) C 1s, (i) C 1s.

N_2 adsorption/desorption isotherms tests are done to calculate specific surface area of pure NPs and rGO/MF (M = Cu, Co, Ni) nanohybrids. As shown in Table 1, the BET value of rGO/MF (M = Cu, Co, Ni) is much higher than that of pure NPs, indicating that rGO sheets improved the dispersion of the NPs, which may resulting its improved catalytic activity.

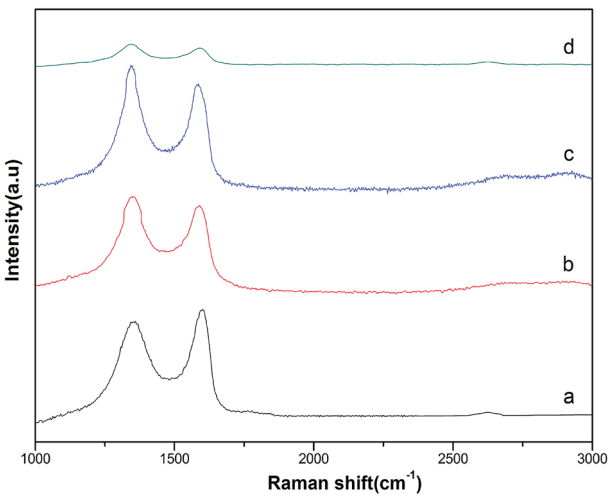

Fig. 5 Raman spectra of (a) GO, (b) rGO/CuF, (c) rGO/CoF and (d) rGO/NiF nanohybrids.

3.2 The catalytic effect of the rGO/MFe_2O_4 (M = Cu, Co, Ni) nanohybrids on the thermal decomposition of AP

To investigated the catalytic behaviors of the catalysts, TG-DSC curves were tested at a heating rate of 10 °C min^{-1}. Fig. 6a shows DSC curves of pure AP. It indicates a three-stage decomposition process. In the first stage, peak centered at 247.4 °C, is in

Table 1 Specific surface area of rGO/MF (M = Cu, Co, Ni) and pure NPs nanohybrids

Sample	BET surface area (m^2 g^{-1})
rGO/CuF	94.60
rGO/CoF	74.79
rGO/NiF	73.92
CuF	33.01
CoF	26.74
NiF	26.53

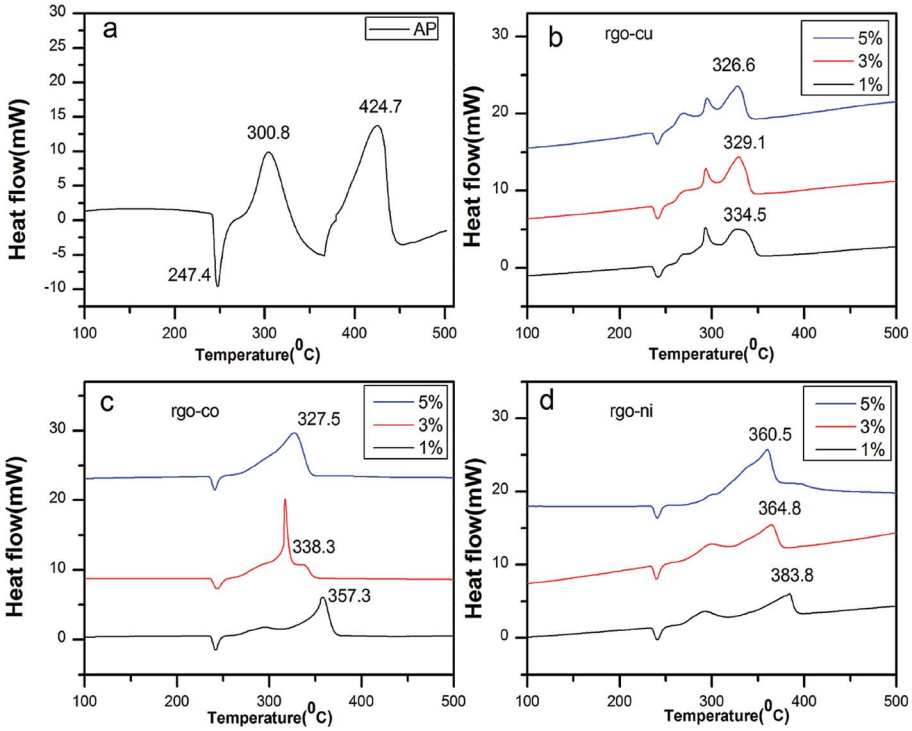

Fig. 6 DSC curves of (a) pure AP, AP mixed with (b) rGO/CuF, (c) rGO/CoF, and (d) rGO/NiF (1 wt%, 3 wt%, 5 wt%) nanohybrids.

agreement with crystallographic transition from the orthorhombic to cubic form. In the second stage, peaks at 300.8 °C, shows low-temperature decomposition (LTD) and peaks at 424.7 °C shows high-temperature decomposition (HTD).

However, Fig. 6b–d show the endothermic peak has no shifts, indicating that rGO/MFe_2O_4 nanohybrids have no impact on the endothermic process but obvious peak temperature decreasing is taken place in LTD and HTD process.

In Fig. 6b, LTD peak has no significant changes. As shown in Fig. 6c and d, only one exothermic peak (HTD peak) is obvious for 5 wt%, compared with two exothermic peaks for 1 wt% and 3 wt%. The HTD peak temperature of AP/rGO/MFe_2O_4 (M = Cu, Co, Ni) mixtures are reduced by 90.2 °C, 67.4 °C, 40.9 °C (1 wt%), 95.6 °C, 86.4 °C, 59.9 °C (3 wt%), 98.1 °C, 97.2 °C, 64.2 °C (5 wt%), respectively. Meanwhile, the released energy of the mixtures (3% wt) is 1523.5 J g^{-1}, 1376.7 J g^{-1} and 1248.3 J g^{-1}, increased remarkably compared to 598.3 J g^{-1} of pure AP. The rGO/MFe_2O_4 (M = Cu, Co, Ni) nanohybrids demonstrate excellent catalytic effects in decreasing the HTD temperature and increasing the energy release of AP. However, the rGO/CuF nanohybrids showed the best catalytic effects and the rGO/NiF nanohybrids the least. The thermal catalytic performance of catalysts on the decomposition of AP is content dependent. As seen from Fig. 6, increasing the mass ratio of rGO/MFe_2O_4 (M = Cu, Co, Ni) nanohybrids in mixtures can decrease HTD peak temperature and the catalytic performance of rGO/CuF shows less relative to amounts compared to that of rGO/CoF and rGO/NiF nanohybrids.

For comparison, TG-DSC tests were further conducted to study the catalytic activity of the as-prepared MF (M = Cu, Co, Ni) NPs and rGO sheets at a heating rate of 10 °C min^{-1}. As can be seen in Table 2, rGO/MFe_2O_4 (M = Cu, Co, Ni) nanohybrids demonstrated better catalytic effect than that of pure NPs and rGO.

In Fig. 7a, there are two weight loss steps for pure AP, 23.1% of the first and 76.9% of the second. In Fig. 7b, two weight loss steps take place in all three mass ratio and the weight loss are almost the same, 35.5% of the first and 64.5% of the second. In contrast, Fig. 7c and d show that the weight loss of catalyst (5 wt%) is taken only in one step, which are consistent with their DSC results. Thus the mixtures (5 wt%) exhibit the best catalytic effects in decreasing the HTD temperature of AP compared to other mass ratio. However, for rGO/CuF, it is the most difficult to further decrease the HTD temperature of AP with addition of higher concentration.

3.3 $E_{a,\alpha}$ values of AP mixed with rGO/MFe_2O_4 nanohybrids by model-free methods

To Evaluate the $E_{a,\alpha}$ values of AP mixed with rGO/MFe_2O_4 (3 wt%.) nanohybrids in the HTD process, mixtures were performed at heating rates of 5, 10, 15 and 20 °C min^{-1}.

Table 2 Comparison of the catalytic activity of rGO, pure NPs with the rGO/MFe_2O_4 in the HTD process of AP[a]

Catalyst	ΔT (°C)
$CuFe_2O_4$	71.5
$CoFe_2O_4$	45.4
$NiFe_2O_4$	38.2
rGO	0.9
rGO/$CuFe_2O_4$	95.6
rGO/$CoFe_2O_4$	86.4
rGO/$NiFe_2O_4$	59.9

[a] T: decreased HTD peak temperature.

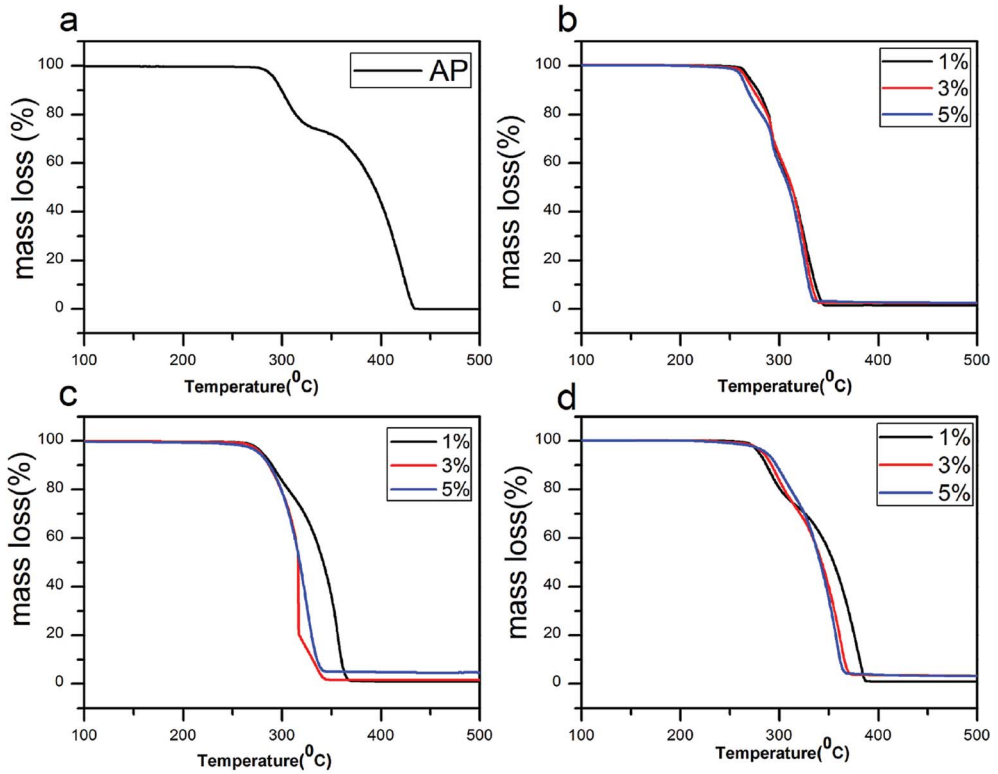

Fig. 7 TG curves of (a) pure AP, AP mixed with (b) rGO/CuF, (c) rGO/CoF and (d) rGO/NiF (1 wt%, 3 wt%, 5 wt%) nanohybrids.

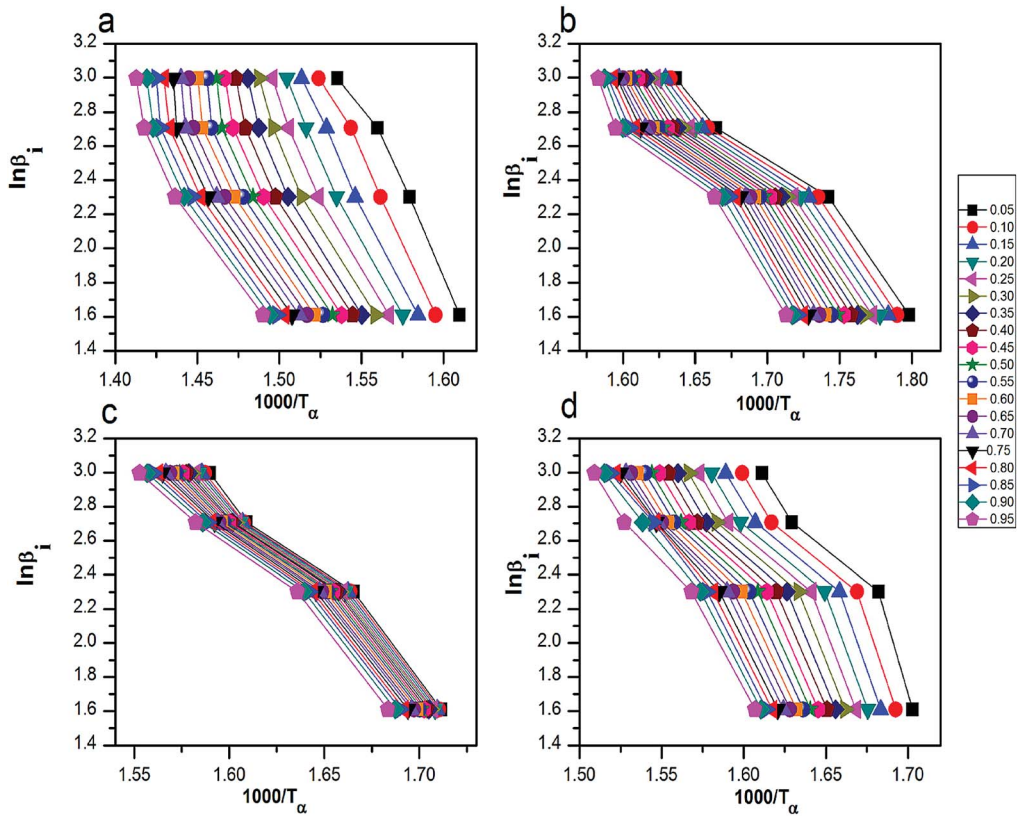

Fig. 8 The curves of $\ln(\beta_i)$ by $1000/T_\alpha$ for thermal decomposition of (a) pure AP, AP mixed with (b) rGO/CuF, (c) rGO/CoF and (d) rGO/NiF (3 wt%) nanohybrids.

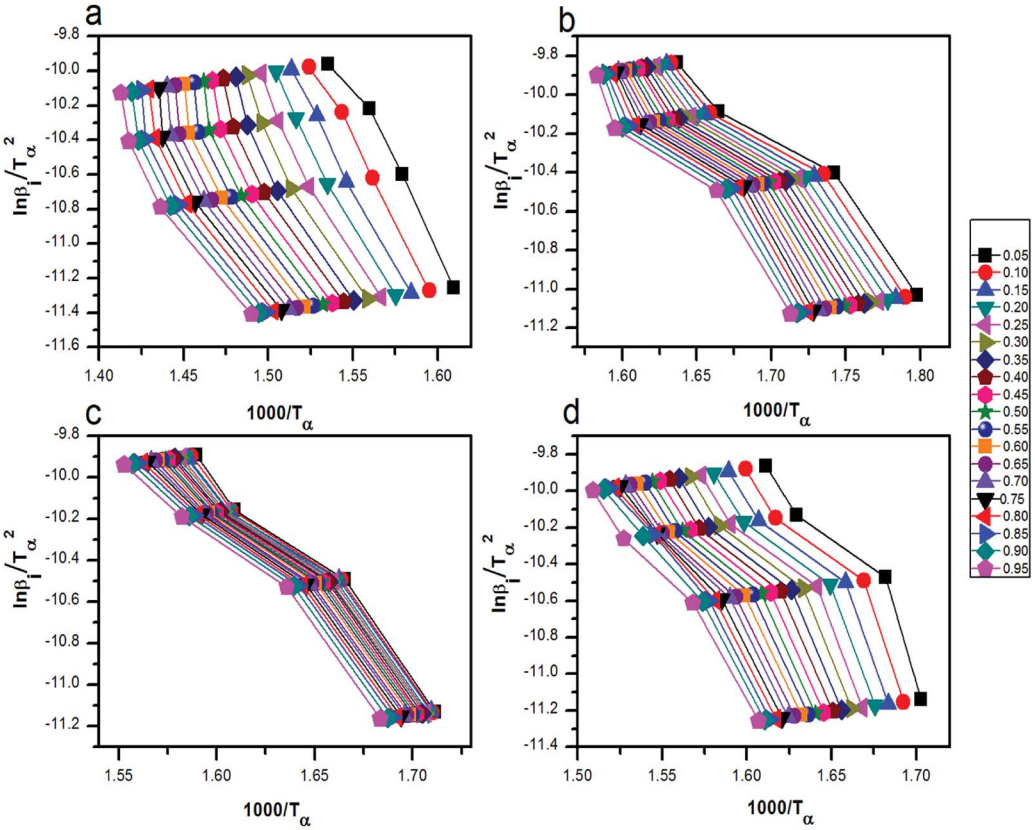

Fig. 9 The curves of $\ln\left(\frac{\beta_i}{T_\alpha^2}\right)$ by $1000/T_\alpha$ for thermal decomposition of (a) pure AP, AP mixed with (b) rGO/CuF, (c) rGO/CoF and (d) rGO/NiF (3 wt%) nanohybrids.

Two model-free methods, Flynn–Wall–Ozawa (FWO) and Kissinger–Akahira–Sunose (KAS) were applied for obtaining $E_{a,\alpha}$ values.[26–33] The two methods allows the activation energy to be evaluated without making any assumptions about the reaction model. Therefore, for the first order reaction, extent of reaction conversion (α) is calculated using the following eqn (1):

Table 3 The HTD $E_{a,\alpha}$ values of pure AP and AP mixed with rGO/MFe_2O_4 (3 wt%) nanohybrids by FWO method

	AP		AP + rGO/CuF		AP + rGO/CoF		AP + rGO/NiF	
α	$E_{a,\alpha}$	R^2	$E_{a,\alpha}$	R^2	$E_{a,\alpha}$	R^2	$E_{a,\alpha}$	R^2
0.05	165.43	0.9696	70.29	0.9503	94.03	0.96339	116.43	0.8725
0.10	173.36	0.9924	72.14	0.9504	93.19	0.96468	115.84	0.8910
0.15	172.27	0.9965	73.70	0.9541	93.07	0.96687	115.63	0.9018
0.20	169.93	0.9905	74.58	0.9548	92.85	0.96735	115.52	0.9082
0.25	166.51	0.9790	75.54	0.9548	92.47	0.9683	115.74	0.9139
0.30	164.59	0.9668	76.19	0.9542	92.10	0.96921	116.19	0.9210
0.35	165.33	0.9585	77.03	0.9515	91.74	0.96797	116.12	0.9290
0.40	160.27	0.9501	77.78	0.9526	91.60	0.96761	116.65	0.9362
0.45	159.37	0.9427	79.05	0.9490	91.52	0.96962	116.76	0.9396
0.50	157.77	0.9308	79.58	0.9489	91.30	0.96995	117.19	0.9448
0.55	157.12	0.9270	80.32	0.9466	91.08	0.97026	118.24	0.9495
0.60	156.00	0.9281	81.07	0.9441	91.00	0.97008	118.23	0.9540
0.65	153.58	0.9225	81.93	0.9437	91.06	0.97147	119.19	0.9607
0.70	153.27	0.9219	82.57	0.9418	90.66	0.97029	120.85	0.9628
0.75	151.90	0.9165	83.45	0.9397	90.85	0.97112	123.23	0.9710
0.80	150.99	0.9251	83.87	0.9383	90.52	0.97035	125.31	0.9732
0.85	149.98	0.9184	84.10	0.9396	90.32	0.96907	126.96	0.9733
0.90	148.55	0.9259	84.53	0.9397	90.02	0.96887	125.21	0.9779
0.95	145.19	0.9299	84.55	0.9420	89.82	0.9679	119.40	0.9764

Table 4 The HTD $E_{a,\alpha}$ values of pure AP and AP mixed with rGO/MFe_2O_4 (3 wt%) nanohybrids by KAS method

	AP		AP + rGO/CuF		AP + rGO/CoF		AP + rGO/NiF	
α	$E_{a,\alpha}$	R^2	$E_{a,\alpha}$	R^2	$E_{a,\alpha}$	R^2	$E_{a,\alpha}$	R^2
0.05	154.31	0.9649	60.10	0.9320	83.43	0.9534	105.87	0.8725
0.10	162.15	0.9913	61.91	0.9327	82.58	0.9549	105.21	0.8910
0.15	160.99	0.9961	63.44	0.9381	80.89	0.9535	104.94	0.9018
0.20	158.58	0.9892	64.30	0.9391	82.22	0.9582	104.78	0.9082
0.25	155.10	0.9760	65.23	0.9394	81.84	0.9593	104.94	0.9139
0.30	153.12	0.9620	65.85	0.9387	81.45	0.9604	105.35	0.9210
0.35	153.80	0.9524	66.67	0.9353	81.08	0.9588	105.24	0.9290
0.40	148.69	0.9426	67.40	0.9370	80.94	0.9583	105.73	0.9362
0.45	147.73	0.9340	68.64	0.9325	80.85	0.9608	105.81	0.9396
0.50	146.10	0.9201	69.15	0.9325	80.62	0.9612	106.20	0.9448
0.55	145.40	0.9156	69.87	0.9296	80.39	0.9616	107.22	0.9495
0.60	144.23	0.9168	70.59	0.9266	80.30	0.9613	107.18	0.9540
0.65	141.77	0.9091	71.43	0.9262	80.35	0.9631	108.11	0.9607
0.70	141.43	0.9093	72.06	0.9239	79.93	0.9615	109.76	0.9628
0.75	140.02	0.9029	72.91	0.9215	80.12	0.9625	112.11	0.9710
0.80	139.07	0.9128	73.31	0.9198	79.77	0.9615	114.17	0.9732
0.85	138.02	0.9048	73.52	0.9214	79.56	0.9598	115.80	0.9733
0.90	136.55	0.9134	73.93	0.9216	79.24	0.9594	114.02	0.9779
0.95	133.15	0.9177	73.92	0.9245	79.01	0.9581	108.17	0.9764

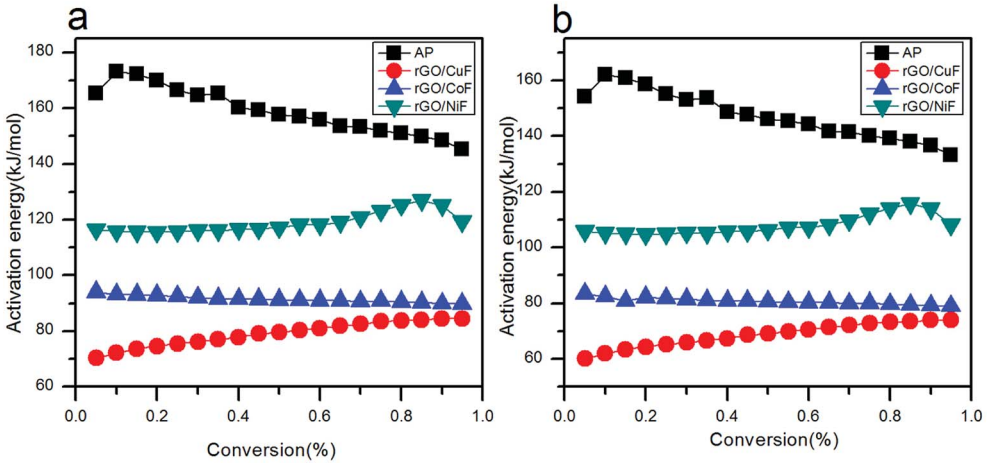

Fig. 10 Dependence of $E_{a,\alpha}$ with α according to (a) FWO method, (b) KAS method for the decomposition of AP mixed with rGO/MFe_2O_4 nanohybrids.

$$\alpha = \frac{m_0 - m_t}{m_0 - m_\infty} \quad (1)$$

The m_0 and m_t are the mass of the sample at the starting and ending time; while m_∞ is the mass at arbitrary time or temperature.

The FWO method shown in eqn (2) is:

$$\ln(\beta_i) = \text{const} - 1.0518\frac{E_{a,\alpha}}{RT_\alpha} \quad (2)$$

The KAS method shown in eqn (3) is:

$$\ln\left(\frac{\beta_i}{T_\alpha^2}\right) = \text{const} - \frac{E_{a,\alpha}}{RT_\alpha} \quad (3)$$

where β_i is heating rate, $E_{a,\alpha}$ is activation energy, R is ideal gas constant, T_α is temperature at arbitrary conversion values. Fig. 8 and 9 show the experimentally measured $\ln(\beta_i)$ *versus* $1000/T_\alpha$ and $\ln\left(\frac{\beta_i}{T_\alpha^2}\right)$ *versus* $1000/T_\alpha$ with rGO/MFe_2O_4 nanohybrids, respectively.

The relationship of E_a to extent of conversion are calculated by FWO and KAS methods in HTD process. The E_a values and its corresponding linear correlation coefficient (R^2) for conversion values from 0.05 to 0.95, are shown in Tables 3 and 4. The dependence of E_a on α using FWO and KAS method is shown in Fig. 10, respectively. Since the $E_{a,\alpha}$ values of mixtures have increased, HTD process of AP is done harder and slower.

3.4 Catalytic mechanism

According to the previous researches,[34] the first decomposition stage is solid–gas multiple reaction including decomposition and sublimation:

$$NH_4ClO_4 \rightarrow NH_4^+ + ClO_4^- \quad (4)$$

$$MFe_2O_4 \rightarrow MFe_2O_4\,(h^+ + e^-) \quad (5)$$

$$Fe^{3+} + ClO_4^- \rightarrow Fe^{2+} + ClO_4 \quad (6)$$

$$Fe^{2+} + NH_4^+ \rightarrow Fe^{3+} + NH_4 \quad (7)$$

$$MFe_2O_4\,(e^-) + rGO \rightarrow MFe_2O_4 + rGO\,(e^-) \quad (8)$$

Once the mixture of AP and rGO/MFe_2O_4 is heated, electrons in the valence band (VB) of MFe_2O_4 can jump to its conduction band (CB), meanwhile the generation of holes (h^+) in the VB is coming. MFe_2O_4 provide easy access to transfer electrons from ClO_4^- to NH_4^+. Because rGO are known as good electron acceptors,[35] the electrons are transferred to the rGO rapidly *via* a percolation mechanism. rGO/MFe_2O_4 were used as catalysts for the decomposition, which can prevent the electrons and holes of MFe_2O_4 recombining, and then boost the dissociation of ClO_4^-, thus leading to the enhanced catalytic effect.

4. Conclusion

rGO/MFe_2O_4 (M = Cu, Co, Ni) nanohybrids have been successfully prepared by a facile hydrothermal way to prevent the agglomeration of NPs. The CuF, CoF, NiF NPs are homogeneously dispersed on rGO sheets. DSC results indicate that the rGO/CuF, rGO/CoF, rGO/NiF nanohybrids (3 wt%), can decrease the HTD peak temperature of pure AP from 424.7 °C to 329.1 °C, 338.3 °C, 364.8 °C, respectively, and enhance catalytic performance with increasing amount. The two methods are used to estimate the values of E_a from TG tests without applying the model. Each activation energy has a separate value at different α. According to the FWO method, the $E_{a,\alpha}$ values (α = 0.45) of AP with rGO/CuF, rGO/CoF, rGO/NiF nanohybrids are reduced from 159.37 kJ mol^{-1} of pure AP to 79.05 kJ mol^{-1}, 91.52 kJ mol^{-1}, 116.76 kJ mol^{-1}, respectively. As for the KAS method, the values are from 147.73 kJ mol^{-1} to 68.64 kJ mol^{-1}, 80.85 kJ mol^{-1}, 116.76 kJ mol^{-1}, respectively. The enhanced catalytic activity, attributed to the synergistic effect of NPs and rGO, can make the rGO/MFe_2O_4 (M = Cu, Co, Ni) nanohybrids be promising catalysts in the AP-based propellants or energetic materials.

Conflicts of interest

There are no conflicts to declare.

Acknowledgements

This research was supported by the International Science & Technology Cooperation Program of China (2014DFR61080).

References

1 R. A. Isbell and M. Q. Brewster, Optical properties of energetic materials: RDX, HMX, AP, NC/NG, and HTPB, *Propellants, Explos., Pyrotech.*, 1998, **23**, 218–224.

2 D. M. Badujar, M. B. Talawar, S. N. Asthana and P. P. Mahulikar, Advances in Science and Technology of Modern Energetic Materials: an Overview, *J. Hazard. Mater.*, 2008, **151**, 289–305.

3 S. G. Hosseini, R. Ahmadi, A. Ghavi and A. Kash, Synthesis and characterization of α-Fe_2O_3 mesoporous using SBA-15 silica as template and investigation of its catalytic activity for thermal decomposition of ammonium perchlorate particles, *Powder Technol.*, 2015, **278**, 316.

4 X. L. Luo, Y. F. Han, D. S. Yang and Y. S. Chen, Solvo-thermal synthesis of Cu_2O micro-spheres and their catalytic performance for thermal decomposition of ammonium perchlorate, *Acta Phys.-Chim. Sin.*, 2012, **28**, 297.

5 A. A. Said and R. A. Qasmi, The role of copper cobaltite spinel, $Cu_xCo_{3-x}O_4$ during the thermal decomposition of ammonium perchlorate, *Thermochim. Acta*, 1996, **275**, 83–91.

6 W. F. Chen, F. S. Li, J. X. Liu, H. C. Song and J. Y. Yu, Preparation of nanocrystalline Co_3O_4 and its catalytic performance for thermal decomposition of ammonium perchlorate, *Chin. J. Catal.*, 2005, **26**, 1073–1077.

7 N. Li, M. H. Cao, Q. Y. Wu and C. W. Hu, A facile one-step method to produce Ni/graphene nanocomposites and their application to the thermal decomposition of ammonium perchlorate, *CrystEngComm*, 2012, **14**, 428–434.

8 N. Li, Z. F. Geng, M. H. Cao, L. Ren, X. Y. Zhao, B. Liu, Y. Tian and C. W. Hu, Well-dispersed ultrafine Mn_3O_4 nanoparticles on graphene as a promising catalyst for the thermal decomposition of ammonium perchlorate, *Carbon*, 2013, **54**, 124–132.

9 G. Tang, Y. W. Wen, A. M. Pang, D. W. Zeng, Y. G. Zhang, S. Q. Tian, B. Shan and C. S. Xie, The atomic origin of high catalytic activity of ZnO nano tetrapods for decomposition of ammonium perchlorate, *CrystEngComm*, 2014, **16**, 570–574.

10 H. Gleiter, Nanocrystalline materials, *Prog. Mater. Sci.*, 1989, **33**, 223–315.

11 Y. Yuan, W. Jiang, Y. Wang, P. Shen, F. Li, P. Li, F. Zhao and H. Gao, Hydrothermal preparation of Fe_2O_3/graphene nanocomposite and its enhanced catalytic activity on the thermal decomposition of ammonium perchlorate, *Appl. Surf. Sci.*, 2014, **303**, 354–359.

12 N. Li, Z. Geng, M. Cao, L. Ren, X. Zhao, B. Liu, Y. Tian and C. Hu, Well-dispersed ultrafine Mn_3O_4 nanoparticles on graphene as a promising catalyst for the thermal decomposition of ammonium perchlorate, *Carbon*, 2013, **54**, 124–132.

13 G. Eda and M. Chhowalla, Graphene Patchwork, *ACS Nano*, 2011, **5**, 4265.

14 P. V. Kamat, Graphene-Based Nanoarchitectures. Anchoring Semiconductor and Metal Nanoparticles on a Two-Dimensional Carbon Support, *J. Phys. Chem. Lett.*, 2010, **1**, 520–527.

15 Z. S. Wu, W. C. Ren, L. Wen, L. B. Gao, J. P. Zhao, Z. P. Chen, G. M. Zhou, F. Li and H. M. Cheng, Graphene Anchored with Co_3O_4 Nanoparticles as Anode of Lithium Ion Batteries with Enhanced Reversible Capacity and Cyclic Performance, *ACS Nano*, 2010, **4**, 3187–3194.

16 W. Hummer and R. Offeman, Preparation of graphitic oxide, *J. Am. Chem. Soc.*, 1958, **80**, 1339.

17 A. Eslami, S. G. Hosseini and V. Asadi, The effect of microencapsulation with nitrocellulose on thermal properties of sodium azide particles, *Prog. Org. Coat.*, 2009, **65**, 269–274.

18 S. J. Park, K. S. Lee, G. Bozoklu, W. W. Cai, S. T. Nguyen and R. S. Ruoff, Graphene oxide papers modified by divalent ions—enhancing mechanical properties *via* chemical cross-link, *ACS Nano*, 2008, **2**, 572–578.

19 Y. S. Fu and X. Wang, Magnetically Separable $ZnFe_2O_4$–Graphene Catalyst and its High Photocatalytic Performance under Visible Light Irradiation, *Ind. Eng. Chem. Res.*, 2011, **50**, 7210–7218.

20 S. A. Chambers, R. F. C. Farrow, S. Maat, M. F. Toney, L. Folks, J. G. Catalano, T. P. Trainor and G. E. Brown Jr, Molecular beam epitaxial growth and properties of $CoFe_2O_4$ on MgO(001), *J. Magn. Magn. Mater.*, 2002, **246**, 124–139.

21 I. Nedkov, R. E. Vandenberghe, T. Marinova, P. Thailhades, T. Merodiiska and I. Avramova, Magnetic structure and collective Jahn-Teller distortions in nanostructured particles of $CuFe_2O_4$, *Appl. Surf. Sci.*, 2006, **253**, 2589–2596.

22 T. Yamashita and P. Hayes, Analysis of XPS spectra of Fe^{2+} and Fe^{3+} ions in oxide materials, *Appl. Surf. Sci.*, 2008, **254**, 2441–2449.

23 M. Fu, Q. Z. Jiao and Y. Zhao, Preparation of NiFe2O4 nanorod-graphene composites *via* an ionicliquid assisted one-step hydrothermal approach and their microwave absorbing properties, *J. Mater. Chem.*, 2013, **A1**, 5577–5586.

24 H. Estrade-Szwarckopf, XPS photoemission in carbonaceous materials: a "defect" peak beside the graphitic asymmetric peak, *Carbon*, 2004, **42**, 1713–1721.

25 S. Stankovich, D. A. Dikin, R. D. Piner, K. A. Kohlhaas, A. Kleinhammes, Y. Jia, Y. Wu, S. T. Nguyen and R. S. Ruoff, Synthesis of graphene-based nanosheets *via* chemical reduction of exfoliated graphite oxide, *Carbon*, 2007, **45**, 1558–1565.

26 J. M. Criado, L. A. Perez-Maqueda and P. E. Sanchez-Jimenez, Dependence of the pre exponential factor on temperature, *J. Therm. Anal. Calorim.*, 2005, **82**, 671–675.

27 Z. Shuping, W. Yulong, Y. Mingde, L. Chun and T. Junmao, Pyrolysis characteristics and kinetics of the marine

microalgae Dunaliellatertiolecta using thermogravimetric analyzer, *Bioresour. Technol.*, 2010, **101**, 359–365.

28 S. Syed, R. Qudaih, I. Talab and I. Janajreh, Kinetics of pyrolysis and combustion of oil shale sample from thermogravimetric data, *Fuel*, 2011, **90**, 1631–1637.

29 P. Murugan, N. Mahinpey, T. Mani and N. Freitag, Pyrolysis and combustion kinetics of Fostert on oil using thermogravimetric analysis, *Fuel*, 2009, **88**, 1708–1713.

30 M. Muthuraman, T. Namioka and K. Yoshikawa, Characteristics of co-combustion and kinetic study on hydrothermally treated municipal solid waste with different rank coals: a thermogravimetric analysis, *Appl. Energy*, 2010, **87**, 141–148.

31 C. Chen, X. Ma and K. Liu, Thermogravimetric analysis of microalgae combustion under different oxygen supply concentrations, *Appl. Energy*, 2011, **88**, 3189–3196.

32 Y. Chunmiao, Y. Lifu, L. Chang, L. Gang and Z. Shengjun, Thermal analysis of magnesium reactions with nitrogen/oxygen gas mixtures, *J. Hazard. Mater.*, 2013, **260**, 707–714.

33 H. Mostaan, F. Karimzadeh and M. H. Abbasi, Non-isothermal kinetic studies on the formation of Al_2O_3/Nb composite, *Thermochim. Acta*, 2010, **511**, 32–36.

34 L. L. Bircumshaw and B. H. Newmann, The thermal decomposition of ammonium perchlorate I. Introduction, experimental, analysis of gaseous products, and thermal decomposition experiments, *Proc. R. Soc. A*, 1954, **227**, 115–132.

35 I. V. Lightcap, T. H. Kosel and P. V. Kamat, Anchoring Semiconductor and Metal Nanoparticles on a Two-Dimensional Catalyst Mat. Storing and Shuttling Electrons with Reduced Graphene Oxide, *Nano Lett.*, 2010, **10**, 577–583.